Calibration of Panoramic Terrestrial Laser Scanners using Planar Patches

Eike Koller[1], Lasse Klingbeil[2], Heiner Kuhlmann[3]

[1]Institute of Geodesy and Geoinformation, University of Bonn, Germany - e.koller@igg.uni-bonn.de
[2]Institute of Geodesy and Geoinformation, University of Bonn, Germany - lasse.klingbeil@uni-bonn.de
[3]Institute of Geodesy and Geoinformation, University of Bonn, Germany - heiner.kuhlmann@uni-bonn.de

Keywords: Terrestrial Laser Scanning, Quality Assessment, Calibration

Abstract

Using point clouds captured by Terrestrial Laser Scanners for measurement tasks with high-quality requirements is well established in engineering geodesy. However, mechanical imperfections within the scanners introduce systematic deviations into the captured point clouds, exceeding the impact of random measurement noise. Calibrating the scanners by estimating these internal imperfections allows these systematic errors to be corrected, thereby preventing misinterpretations of the measurement results. In this work, we implement a methodology that allows users of Terrestrial Laser Scanners to independently determine calibration parameters for panorama scanners and to correct the resulting point clouds using planar patches extracted directly from the captured data. Our work extends existing approaches by using a comprehensive calibration model of the National Institute of Standards and Technology (NIST), including all existing 18 calibration parameters. It relies on a network-based method to estimate transformations between TLS stations, utilizing plane parameters. In this process, calibration parameters are included as supplementary parameters. Additionally, we evaluate the methodology using a real-world point cloud of a water dam and demonstrate that it achieves a substantial reduction in systematic deviations in the magnitude of several millimeters, so that mainly random noise remain. Furthermore, by estimating calibration parameters within a dedicated state-of-the-art calibration field, we demonstrate that our method achieves a reduction in systematic errors comparable in magnitude to established calibration procedures. Although the nominal values of the estimated calibration parameters differ due to correlations among parameters, this performance is obtained without requiring specialized calibration environments.

1. Introduction

Structural health monitoring of critical infrastructure represents a core discipline of modern engineering geodesy. Terrestrial Laser Scanners (TLS) are increasingly employed to enable the early detection of deformations (Teng et al., 2022). These sensors can rapidly generate highly accurate and high-resolution point clouds in large-scale areas, which represent the surface geometry of the monitored object (Vosselman and Maas, 2010; Schwarz, 2018). Unlike point-based techniques such as tacheometry or using Global Navigation Satellite Systems (GNSS), using TLS allows even unexpected deformations to be detected (Holst and Kuhlmann, 2016). TLS point clouds capture the entire surface of an object, allowing comprehensive structural monitoring without the need to mark discrete object points, whose targeted selection would otherwise require a priori knowledge of the expected deformation.

In addition to random measurement deviations, TLS point clouds can also contain systematic deviations. On the one hand, point clouds are systematically influenced by prevailing atmospheric conditions, the measurement geometry and the measurement object itself. On the other hand, internal mechanical misalignments due to the manufacturing process, temperature changes, aging, etc., also cause systematic effects (Soudarissanane et al., 2011; Medić et al., 2021).

These effects complicate the interpretation of point clouds in terms of potential deformations: if the influence of mechanical misalignments on the point cloud exceeds the magnitude of the actual deformation, genuine structural changes can no longer be distinguished from systematic measurement errors, preventing meaningful deformation analysis. TLS calibration allows for the correction of mechanical misalignments, thereby reducing systematic errors and enabling a more reliable interpretation of point clouds with respect to potential deformations (Jost et al., 2023).

The aim of TLS calibration is to determine a set of calibration parameters (CPs) within a functional model that describes the influence of mechanical misalignments on the polar observations (range, horizontal angle and vertical angle) of the instrument. Using this model and the estimated CPs, the polar observations and consequently the resulting point clouds can be corrected for systematic effects without the need for any mechanical adjustment of the scanner itself. In particular, before conducting measurement tasks with high accuracy requirements—such as deformation monitoring—the CPs should be determined individually.

Many studies determine CPs using TLS targets scanned from one or more stations. By designing a measurement geometry that is particularly sensitive to systematic deviations caused by internal misalignments, CPs can be derived through various approaches. Muralikrishnan et al. (2015) and Shi et al. (2020) employ targets with precisely known distances. This approach requires reference standards or auxiliary instruments, such as laser trackers, to measure target distances with an accuracy significantly exceeding that of TLS precision. As an alternative, e.g Wang et al. (2017) and Muralikrishnan et al. (2018) apply length consistency tests, in which targets are scanned from multiple stations. CPs are then inferred from the observed changes in distance caused by systematic scanner deviations.

Another option is the network method proposed by Reshetyuk (2009); Wang et al. (2017); Lichti (2007). Here, a set of identical targets is scanned from at least two positions, allowing CPs to be estimated alongside the transformation parameters during a registration process. To decrease the needed number of targets, optimized and dedicated calibration fields can

This contribution has been peer-reviewed. The double-blind peer-review was conducted on the basis of the full paper.
https://doi.org/10.5194/isprs-annals-XI-1-2026-373-2026 | © Author(s) 2026. CC BY 4.0 License.

be established (see Medić et al. (2019b)). A similar approach is taken by Chow et al. (2011), who employs artificially introduced planes within the measurement volume instead of signalized individual points marked by TLS targets.
Additionally, CPs exhibit changes on different time scales (see Medić et al. (2021)). For this reason, Abbas et al. (2014); Medić et al. (2019a); Koller et al. (2025) have developed methods for on-site calibration that can derive CPs directly from scan data of the measured object.
Medić et al. (2020) also concludes that manufacturer calibration alone is insufficient and therefore also evaluates target-based and keypoint-based calibration approaches for improving point cloud quality. However, target-based calibration requires targets in a suitable configuration, while the keypoint-based algorithm relies on strong intensity variations in the scanned objects to detect keypoints and largely ignores geometric information.
Existing work on TLS calibration parameter estimation often requires high-precision normals, numerous targets, highly optimized geometries, or measurement environments that deliver a high variability in intensities. Methods that instead use existing scene geometry, such as planar patches, typically estimate only a reduced set of calibration parameters.
In this work, we present a TLS calibration method based on the network approach using scan points on planar patches, which are often already present in point clouds, especially of anthropogenic objects. This eliminates the need for numerous artificial TLS targets arranged in an optimized configuration to determine CPs, as well as the use of additional sensors or reference normals. It also relies only on the geometry and not on the intensities. Consequently, there is no need for a dedicated calibration field and the approach relies solely on existing structures within the measurement environment, without artificial targets. Therefore, it can be used for on-site calibrations.
In general, our approach is based on the method proposed in Chow et al. (2011) and extends it further. Chow et al. (2011) use a reduced calibration model containing only a few CPs that does not account for all geometric misalignments of modern TLS. In this work, we adopt the calibration model of the National Institute of Standards and Technology (NIST), which comprises 18 parameters that describe a complete calibration model that holds for panoramic TLS (and not for other construction types, which are partially used). As described later, we are able to determine 14 out of the possible 18 parameters with our collected data. Additionally, we incorporate the capability of high-end scanners to perform measurements in front- and back-face. This technique, known from the terminology of total stations, involves scanning the same object with the scanner rotated horizontally by 180°. This ensures that identical cartesian coordinates of the point cloud are physically observed through different angular measurements.
Qiao and Butt (2023) have also proposed an approach based on planar patches. Although the NIST model is applied in this work as well, only a reduced set of 10 CPs is estimated. Furthermore, the CPs are formulated only indirectly through derived observations in the form of M3C2 distances computed from cartesian 3D point clouds. These quantities are composed of multiple measurements and geometric relationships. In contrast, our approach directly employs the polar observations, which particularly facilitates the formulation of the stochastic model. Moreover, the proposed method allows the direct enforcement of planarity requirements for the selected patches, while the approach of Qiao and Butt (2023) only allows this to be considered indirectly.
Furthermore, our contribution demonstrates the influence of the estimated CPs on a real-world dataset through a case study conducted at a dam. Such structures represent typical objects for monitoring applications with high accuracy requirements. Using measurements from a dam, we demonstrate that systematic effects can significantly impact the results, even when using high-end scanners. We further validate our approach by showing that it reduces these systematic effects to a degree comparable with the state-of-the-art method proposed by Medić et al. (2019b).
A comprehensive comparison with all related approaches is beyond the scope of this paper. The selected comparison was chosen because an optimized measurement configuration for the point-based approach is available, which simultaneously contains a large number of planar structures. Our main contributions to the field of TLS calibration are

- implementing a calibration procedure using planar patches without the necessity of artificial targets using the comprehensive calibration model of NIST
- validation of estimated CPs in a typical environment for deformation monitoring (water dam)

We perform calibration measurements using our approach in a calibration facility that contains artificial TLS targets in a configuration developed and optimized by Medić et al. (2019b), which employs a point-based calibration approach. Although a calibration hall is not necessary for our approach, it is used here to directly compare our calibration with one of the state-of-the-art methods, as the same data set can be used for both our approach and that of Medić et al. (2019b). To achieve this, we extend the calibration model used in Medić et al. (2019b) to 14 parameters, since it is based on the NIST model but includes only 10 parameters.
The following work is structured as follows: Chapter 2 introduces the NIST calibration model used and describes the methodology of TLS calibration with our plane-based approach and point-based approach. In chapter 3, we present the environment for calibration and the water dam including the collection and the preprocessing of the data. The obtained CPs are discussed in chapter 4, applied to a real dam, and evaluated. Finally, chapter 5 summarizes the results obtained and provides an outlook.

2. Methodology

Every TLS observation is systematically influenced by mechanical misalignments, which are mathematically modeled using calibration models with corresponding CPs. The aim of this work is to determine this CPs of the calibration model specifically for each scanner. For this purpose, there must be a functional relationship between the TLS observations and the mechanical misalignments.

2.1 Impact of Calibration Parameters

In order to obtain a Point i from Station j, TLS observe distances r_i^j, horizontal angles φ_i^j and vertical angles θ_i^j. From these polar measurements, the cartesian coordinates $\mathbf{X}_i^j$ can be calculated according to Schwarz (2018) with

$$\mathbf{X}_i^j = \begin{bmatrix} x_i^j \\ y_i^j \\ z_i^j \end{bmatrix} = \begin{bmatrix} r_i^j \cdot \sin\theta_i^j \cdot \cos\varphi_i^j \\ r_i^j \cdot \sin\theta_i^j \cdot \sin\varphi_i^j \\ r_i^j \cdot \cos\theta_i^j \end{bmatrix}. \quad (1)$$

CP	Description
x_{1n}, $x_{1z}*$	hor.l/vert. beam offset
x_2*	hor. axis offset
x_3*	mirror offset
x_4*	vert. index offset
x_{5n}, $x_{5z}*$	hor./vert. beam offset
x_6*	mirror tilt
x_7*	hor. axis tilt
$x_{8x}*$, $x_{8y}*$	hor. angle encoder eccentricity
$x_{9n}*$, x_{9z}	vert. angle encoder eccentricity
x_{10}	rangefinder offset
x_{11a}, x_{11b}	2^{nd} order scale error (hor.)
$x_{12a}*$, x_{12b}	2^{nd} order scale error (ver.)

Table 1. Parameters of geometric error model developed by NIST. (.)* indicates two-face sensitivity.

Any mechanical misalignment affects one or more of the polar elements. To describe this effect, we use the model developed by the National Institute of Standards and Technology (NIST) (Wang et al., 2017). This comprehensive geometric error model comprises a set of 18 CPs, which are listed in Table 1. The aim of TLS calibration is to obtain these parameters. Due to the measuring principle of TLS, CPs exhibit opposing effects when observing from front-face or from back-face. CPs whose signs change between the faces are denoted with an asterisk (.)*. The influence of these CPs on the polar elements is described by Equations 2 - 4. For front-face observations, $\gamma = 1$ applies; analogously, for back-face measurements, $\gamma = -1$ applies.

$$\Delta r_i^j = \gamma\Big(x_2 \sin\theta_i^j + x_{10}\Big) \tag{2}$$

$$\begin{aligned}\Delta\varphi_i^j = \gamma\Big(&\frac{x_{1z}}{r_i^j \tan\theta_i^j} + \frac{x_3}{r_i^j \sin\theta_i^j} + \frac{x_{5z}}{\tan\theta_i^j} + \frac{2x_6}{\sin\theta_i^j} \\ &- \frac{x_7}{\tan\theta_i^j} - x_{8x}\sin\varphi_i^j + x_{8y}\cos\varphi_i^j\Big) \\ &+ \frac{x_{1n}}{r_i^j} + x_{5n} + x_{11a}\cos 2\varphi_i^j + x_{11b}\sin 2\varphi_i^j\end{aligned} \tag{3}$$

$$\begin{aligned}\Delta\theta_i^j = \gamma\Big(&\frac{x_{1n}\cos\theta_i^j}{r_i^j} + \frac{x_2\cos\theta_i^j}{r_i^j} + x_4 + x_{5n}\cos\theta_i^j \\ &+ x_{9n}\cos\theta_i^j\Big) - \frac{x_{1z}\sin\theta_i^j}{r_i^j} - x_{5z}\sin\theta_i^j - \\ &x_{9z}\sin\theta_i^j + x_{12a}\cos 2\theta_i^j + x_{12b}\sin 2\theta_i^j\end{aligned} \tag{4}$$

2.2 Plane-Based Approach

The plane-based approach employs the network method to determine the CPs. This requires point clouds that contain corresponding planar patches k from at least two stations. The transformation of the scanned point $\mathbf{X}_k^j$ of the planar patch k of Station j to Station 1 is defined by Equation 5 (Chow et al., 2011)

$$\mathbf{f}_k = \mathbf{n}_k^T(\mathbf{R}(\omega^j, \phi^j, \kappa^j)\mathbf{X}_k^j + \begin{bmatrix}t_x^j & t_y^j & t_z^j\end{bmatrix}^T - d_k = \mathbf{0}. \tag{5}$$

Here, $\mathbf{n}_k$ and d_k describe the normal vector and the offset parameter of the planar patch k in the scan of Station 1, t_x, t_y and t_z are the entries of the translation vector and $\mathbf{R}$ defines the rotation matrix as a function of the euler angles ω, ϕ and κ. To avoid problems caused by ambiguities in the normal vector, $\mathbf{n}_k$ is substituted with $\bar{\mathbf{n}}_k = \mathbf{n}_k/d$ (see Holst et al. (2014)).

It follows that

$$\mathbf{f_k} = \bar{\mathbf{n}}_k^T(\mathbf{R}(\omega^j, \phi^j, \kappa^j)\mathbf{X}_k^j + \begin{bmatrix}t_x^j & t_y^j & t_z^j\end{bmatrix}^T - 1 = \mathbf{0} \tag{6}$$

with $||\bar{\mathbf{n}}_k|| \neq 1$. This functional relationship can be expressed in polar space by substituting Equation 1. Doing this, one can add the impact of the CPs from Equations 2-4 with

$$r_i^j = r_i^j + \Delta r_i^j \tag{7}$$

$$\varphi_i^j = \varphi_i^j + \Delta\varphi_i^j \tag{8}$$

$$\theta_i^j = \theta_i^j + \Delta\theta_i^j \tag{9}$$

to integrate the CPs into the functional model of the transformation given in Equation 6 (Medić et al., 2019b). To re-estimate the polar coordinates from the point cloud, Equation 1 has to be inverted. Many high-end scanners offer the capability of performing front-face and back-face scans. Each back-face scan is then interpreted as a Station j.

We implemented an iterative, nonlinear Gauss-Helmert model to estimate the parameters of the functional model given in Equation 6, namely the CPs, the transformation parameters $\mathbf{T} = \begin{bmatrix}t_x^j & t_y^j & t_z^j\end{bmatrix}$ and $\Phi = \begin{bmatrix}\omega^j & \phi^j & \kappa^j\end{bmatrix}$ and the entries of the substituted normal vectors $\bar{\mathbf{n}}_k$ in a least squares sense according to (Koch, 2013). The required Jacobian $\mathbf{A}$ contains the partial derivatives according to the parameters specified in Equation 10:

$$\mathbf{A} = \begin{bmatrix}\frac{\partial \mathbf{f}_k}{\partial \mathbf{CP}} & \frac{\partial \mathbf{f}_k}{\bar{\mathbf{n}}_k} & \frac{\partial \mathbf{f}_k}{\partial \Phi^j} & \frac{\partial \mathbf{f}_k}{\partial \mathbf{T}^j}\end{bmatrix}, \tag{10}$$

while the Jacobian $\mathbf{B}$ given in Equation 11 contains the partial derivatives of the observations:

$$\mathbf{B} = \begin{bmatrix}\frac{\partial \mathbf{f}_k}{\partial r_i^j} & \frac{\partial \mathbf{f}_k}{\varphi_i^j} & \frac{\partial \mathbf{f}_k}{\partial \theta_i^j}\end{bmatrix}. \tag{11}$$

In this way, we are flexible to choose all CPs or, if necessary, only a subset of CPs to be estimated. To construct $\mathbf{A}$ and $\mathbf{B}$ each point i must be assigned to its corresponding scan j and planar patch k. Unregistered point clouds are used to derive the polar observations directly from the cartesian coordinates by inverting Equation 1. Approximation values for the transformation parameters $\mathbf{T}$ and Φ are obtained from an Iterative-Closest-Points (ICP, see Besl and McKay (1992)) algorithm (without applying the transformation), while the approximation values for the substituted normal vectors $\bar{\mathbf{n}}_k$ are estimated by fitting planes to each patch k in one chosen reference scan using Random Sample Consensus (RANSAC, see Torr and Zisserman (2000)). Other solutions would be conceivable. The approximation values for the CPs are set to zero. The stochastic model is defined in Section 4.1, enabling not only more realistic parameter estimation but also the computation of a-posteriori variances and correlations.

2.3 Point-Based Approach

The calibration procedure used in Medić et al. (2019b) also uses the network method as introduced in Reshetyuk (2009). Here, the transformation between stations is realized by individual corresponding points. Given this set of identical points from a reference Station $\mathbf{X}^{ref}$ and at least one more Station $\mathbf{X}^j$ (e.g. signalized by artificial TLS targets), the following Equation 12

$$\mathbf{f}_i^j = \mathbf{R}(\omega^j, \phi^j, \kappa^j)\mathbf{X}^j + \begin{bmatrix}t_x^j & t_y^j & t_z^j\end{bmatrix}^T - \mathbf{X}^{ref} = \mathbf{0} \tag{12}$$

formulates the transformation between the stations for the point-based approach (Reshetyuk, 2009). Also here, by substituting

Equation 1 and adding the impact of the CPs according to Equation 7-9, one can integrate the CPs into the functional model of the transform. Again, the inversion of Equation 1 can be used to get access to the polar observations from the point cloud. We also use an iterative, nonlinear Gauss-Helmert model to estimate the CPs, transformation parameters and the coordinates $\mathbf{X}^{ref}$ of the reference station in a least squares sense (Koch, 2013).

3. Experimental Setup and Data Acquisition

In this study, CPs are determined using the plane-based approach using the well-established point-based approach within a calibration facility as presented in section 3.1. We also conduct measurements on a dam for the evaluation of CPs.

3.1 Calibration Facility

The calibration facility is located within a machine hall with a area of approximately 25 m x 75 m and a height of 8 m. It contains TLS targets that have been geometrically optimized to enable the determination of CPs using the point-based method described in section 2.3. For this purpose, 14 BOTA8 targets (Janßen et al., 2019) are installed, which can be scanned from two stations in front and back face. A detailed description of the measurement geometry is provided in Medić et al. (2019b). A visual impression of the used environment is given in Figure 1. Owing to its structural design, the calibration facility also

Figure 1. Used Facility to determine CPs containing planar structures and TLS targets in an optimized geometry introduced by Medić et al. (2019b).

contains a variety of planar surfaces, including the floor, rectangular concrete columns along the walls, and wooden stringers on the ceiling. These planar elements exhibit different orientations with respect to the scanner positions.

3.2 Data Collection and Preprocessing for CP Estimation in Calibration Facility

In this study, the CPs of the high-end panoramic TLS *Imager5016* from *Zoller + Fröhlich* are determined and analyzed. For this purpose, a calibration facility containing numerous planar structures, which are used for the plane-based approach, and artificial targets, which are used for the point-based approach, is scanned. We captured point clouds from two stations as described in Medić et al. (2019b) in front and back-face (which results in four scans) with a resolution of *1.6mm@10m*. This resolution ensures a high spatial density of points on both the targets required for the point-based calibration method and the planar patches used in the plane-based approach. The scan quality setting *LOW* was selected to minimize potential influences from internal observation averaging processes. The orientations of the TLS at both stations were arranged orthogonally, as Lichti (2010) demonstrated that such an arrangement reduces correlations between CPs.

Preprocessing for Plane-Based Calibration First, planar surfaces of arbitrary size are manually extracted from one of the four point clouds. We delimit the patch size to 25 cm x 25 cm (see 2.2) to guarantee that mechanical misalignments affect every point on the planar patch equally. This size is selected empirically. Every extracted plane, which exhibits a larger size, is automatically divided into patches of the desired size. The approximately known transformation between the scanner positions allows the corresponding planes to be identified in the remaining three scans, eliminating the need for automatic plane matching based on, e.g., geometric features. To ensure high-quality calibration, specific criteria are imposed on the selected plane patches:

1. Point-to-Plane Deviation: The points of the point cloud must not deviate more than 1 mm from the planar surface. The maximum deviation of an individual point of a patch from an ideal planar surface is ensured by estimating a plane using RANSAC (Torr and Zisserman, 2000) and a threshold of 1 mm through the points of a patch. This procedure is used for outlier removal based on an empirically determined threshold. Therefore, no scanner-specific or material properties are considered.

2. Number of Points on Planar Patch: Every planar patch must contain at least 200 points. If a patch contains fewer than the required number of points, the patch itself and all corresponding patches are removed. The remaining patches are randomly subsampled to a maximum of 350 points to reduce memory consumption and computational effort.

3. Planarity: Each planar patch must have a planarity factor $P \geq 0.7$. We estimate the planarity factor P regarding to Weinmann et al. (2014). For this purpose, the covariance matrix of each patch is computed, and its eigenvalues λ_1, λ_1, and λ_3 are derived. The planarity factor, which quantifies the degree of planarity within the patch, is then calculated as

$$P = \frac{\lambda_2 - \lambda_3}{\lambda_1} \quad with\ P \in [0, 1]. \tag{13}$$

A higher value of P indicates a more planar surface represented by the points. Patches with planarity values below the defined threshold are excluded from further processing.
In this way, 356 planar surfaces can be found in the calibration facility, which can be seen from two stations in front and back-face scans. Figure 2 illustrates the measurement geometry of the planar patches and the scanner, and depicts the relative position of all planar patches with respect to Station 1. The figure visualizes the horizontal angle φ and vertical angle θ of the center point of each planar patch. Planar patches are distributed in all directions around the scanner. Because the ceiling is vaulted, no planar patches can be identified in areas with low zenith angles. Most patches lie on the floor, within $\theta > 100^\circ$ and $\theta < 130^\circ$. Additionally, due to the structural conditions of the calibration facility, a concentration of patches occurs in the horizontal dimension between $\varphi > 75^\circ$ and $\varphi < 105^\circ$.
As shown in equations 2–4, the influence of the calibration parameters on the observations depends on the observations themselves. Therefore, a spatially well-distributed set of observations improves parameter estimation. Our measurement geometry provides azimuthal observations in all directions, although only few observations are available in high elevations.

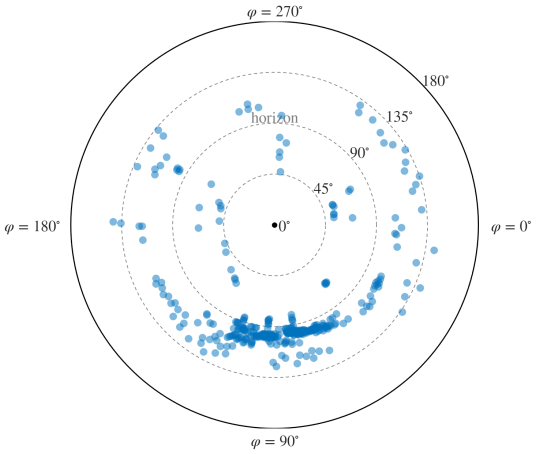

Figure 2. Distribution of planar patches with respect to Station 1. The radial dimension describes the vertical angle θ, the circular direction the horizontal angle φ

CP	plane-based approach		point-based approach	
	$\hat{p}$	$\sigma_{\hat{p}}$	$\sigma_{\hat{p}}$	$\sigma_{\hat{p}}$
x_{1z} $[mm]$	0.19	0.08	0.56	0.03
x_{1n} $[mm]$	1.01	0.08	−0.02	0.02
x_2 $[mm]$	0.05	0.37	0.09	0.05
x_3 $[mm]$	−0.21	0.09	0.13	0.03
x_4 $['']$	28.18	18.05	−13.94	3.81
x_{5z} $['']$	10.18	80.26	−0.94	9.96
x_{5n} $['']$	−57.11	7.35	10.46	1.23
x_6 $['']$	−2.16	8.81	−4.57	2.13
x_7 $['']$	47.97	7.55	28.38	5.24
x_{x10} $[mm]$	1.38	0.08	0.2	0.01
x_{x11a} $['']$	50.95	16.78	−0.69	2.11
x_{x11b} $['']$	−23.81	138.64	1.23	5.24
x_{x12a} $['']$	38.01	16.36	−7.87	5.53
x_{x12b} $['']$	−70.04	16.13	−3.98	3.22

Table 2. Estimated CPs by using the developed plane-based approach and using the state-of-the-art point-based approach.

Preprocessing for Point-Based Calibration All 14 BOTA8 targets are extracted from all captured point clouds, and their target centers are determined following the procedure described in Janßen et al. (2019). The variances of the corresponding polar observations, $[\sigma^2_{r_i}\ \sigma^2_{\varphi_i}\ \sigma^2_{\theta_i}]^T$, are given in an empirically derived model of the BOTA8 targets in Janßen et al. (2019).

3.3 Data Acquisition for Evaluation at the Water Dam

We assess the performance of our determined CPs at a water dam. This environment represents a typical deformation monitoring scenario requiring accurate sensor calibration. The used dam has a crown length of about 200 m and a maximum height of approximately 25 m. Figure 3 provides an overview of the testing environment and the scanning setup, including the scanner position and orientation. The data is captured one

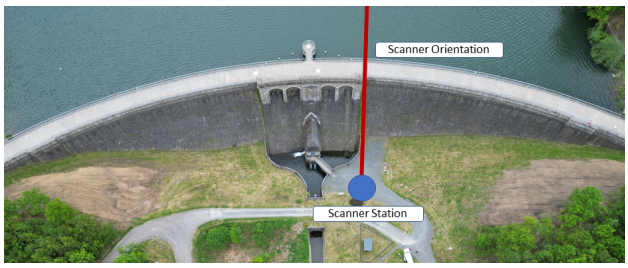

Figure 3. Overview of the test environment.

day after the calibration measurement. A spatial resolution of $3.1mm@10m$ is used with the lowest quality settings in order to minimize the influence of the TLS software on the acquired data. We perform both a front-face and a back-face scan. The orientation of the scanner and thus the position of the change of faces can be seen in Figure 3. The selected position is well-suited for evaluating the calibration as the entire dam can be captured in one scan. High elevations can be realized to maximize the impact of internal misalignment (see equations 2-4).

4. Calibration Results

In this section, we present the obtained CPs by using our plane-based approach and, for comparison by the state-of-the-art point-based approach. Furthermore, the determined CPs are evaluated using an independent point cloud, demonstrating how internal scanner misalignments affect point clouds systematically and how these deviations are reduced when the calculated CPs are applied.

4.1 Estimated CPs

Using the data acquired in the calibration facility as described in section 3.1, we determined CPs using both our plane-based approach following the procedure outlined in 2.2 and the state-of-the-art approach by using the point-based approach as described in 2.3 for comparison. We have defined the front-face scan from Station 1 (s_1^f) as the reference station. Transformation parameters describe the transformation of the back-face scan from Station 1 s_1^b and the remaining scans from Station 2 (s_2^f,s_2^b) to s_1^f. The estimated CPs, called $\hat{p}$, and their corresponding standard deviations $\sigma_{\hat{p}}$ are shown in Table 2. It turned out that the encoder eccentricities represented by the parameters x_{8x}, x_{8y}, x_{9n}, and x_{9z} cannot be estimated reliably with our collected data and the plane-based approach. Numerical values of estimated CPs and standard deviations are of an unexpected magnitude (values and standard deviations greater than $500''$ or the normal equations become singular). A parameter set with numerical values below $100''$ and 2 mm was selected. Therefore, the calibration model is reduced by x_{8x}, x_{8y}, x_{9n}, and x_{9z}, resulting in only 14 CPs being determined instead of the possible 18 (for both the plan-based and point-based approach). As the stochastic model for the adjustment, we adopted manufacturer-specified single-point standard deviations of $\sigma_r = 1.2\,mm$ and $\sigma_\varphi = \sigma_\theta = 8''$ for the plane-based approach. In contrast, the target-based approach employed an empirical model from publication Janßen et al. (2019), which defines the standard deviation of BOTA8 targets as a function of distance. All observations are assumed to be uncorrelated.
The CPs listed in Table 2 for our plane-based approach exhibit varying qualities measured on their a-posteriori standard deviations. While some CPs exhibit standard deviations smaller than the magnitude of the parameter itself, others have standard deviations that exceed the respective parameter value. But the a-posteriori standard deviations strongly depend on the assumed a-priori point accuracy. As correlations between observations were neglected, the estimates are likely optimistic. Moreover, manufacturer specifications refer to instrument series rather than the specific sensor and do not account for influences such as measurement geometry or surface properties. Variance

component estimation was therefore not applied, as measurements on different surfaces affect the observation variances differently and strong parameter correlations (as shown later) may cause variance components to absorb systematic effects (Koch, 2013).

Due to the functional similarity of several CPs, strong correlations occur between the estimated CPs. The top part of Figure 4 visualizes the absolute values of the correlation coefficients $|\rho|$ between the calculated CPs using the plane-based approach. Correlations of up to $|\rho| = 90\%$ in our approach and up to

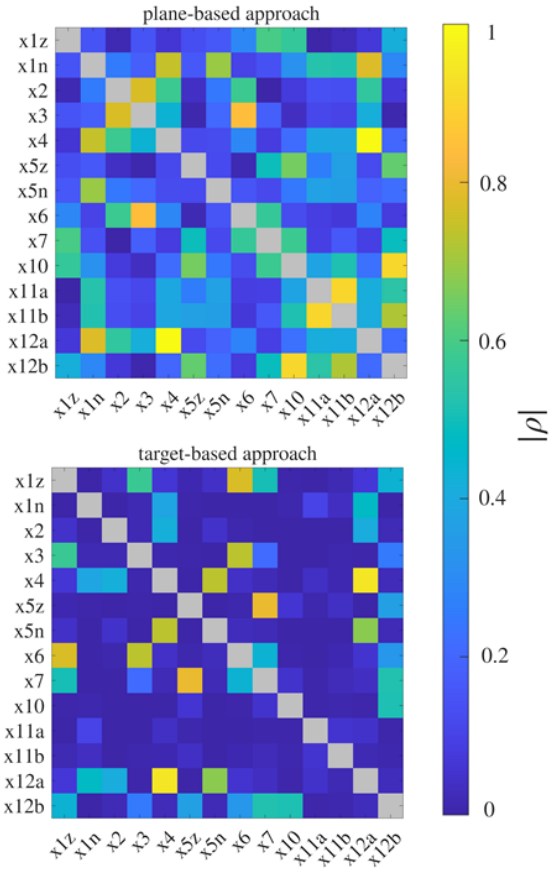

Figure 4. Absolute Correlations Coefficients $|\rho|$ between estimated CPs by using the plane based approach (top part) and point-based approach (bottom part).

$|\rho| = 85\%$ (although these are generally lower) in the point-based approach can be observed between individual parameters. As a result, the CPs cannot be clearly distinguished from one another. Therefore, Wang et al. (2017) recommends to establish $x_{5z7} = x_{5z} - x_7$.

Besides internal misalignments, the measurement data also contain other systematic effects, particularly those arising from the measurement geometry. Factors such as measurement distance and angle of incidence systematically influence each individual point (Soudarissanane et al., 2011) and consequently the plane estimation within the calibration algorithm. These effects are not considered in our approach. As a result, the functional model does not fully capture all systematic influences, which can lead to high correlations between CPs (Kotsakis, 2004).

In addition to the CPs, the transformation parameters between the scans are also estimated. Table 3 presents the differences in these transformation parameters between the two approaches. The registration parameters affect the estimation of the CPs, al-

	$\Delta t_x\ [mm]$	$\Delta t_y\ [mm]$	$\Delta t_z\ [mm]$	$\Delta\omega\ ['']$	$\Delta\phi\ ['']$	$\Delta\kappa\ ['']$
s_1^f	0.1	0.1	1.0	6	2	1
s_2^f	0.0	0.5	0.8	34	5	55
s_2^b	0.2	0.5	0.7	35	5	55

Table 3. Differences of estimated transformation parameters between plane-based and point-based approach.

though this interaction differs between both approaches.

In general, the numerical values of the parameters differ significantly between our approach and the point-based approach. It is also observed that the a-posteriori standard deviations are larger in our method. However, due to high correlations and differences in the registration parameters, the CPs and their quality cannot be directly compared in the parameter space. To assess the practical applicability of the parameters, an evaluation based on a corrected point cloud as described in section 4.2 is therefore required.

4.2 Evaluation of estimated CPs

To illustrate the impact of poorly calibrated TLS, we performed an M3C2 point cloud comparison between front and back-face scans of the collected data at the water dam presented in 3.3 as an (from the calibration measurement) independent dataset. As shown in Table 1, the sign of the impact of some CP changes in front- and back-face, so their effects can be visualized through this comparison. To similarly assess CPs that are not sensitive to both faces, point cloud comparisons from different stations would be required. However, in such cases, influences from measurement geometry, atmospheric conditions, and the necessary registration process would dominate, obscuring the effects due to calibration.

Figure 5a) shows the M3C2 comparison of point clouds from the two faces for uncalibrated point clouds. High systematic

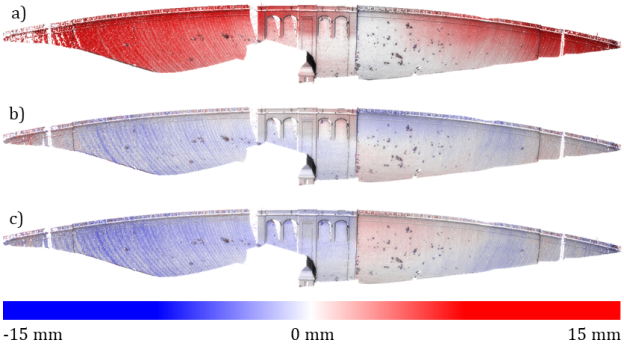

Figure 5. M3C2 differences of measured point clouds at the water dam in front and back-face of the uncalibrated point cloud (a) and the calibrated point cloud using plane-based (b) and point-based (c) approach.

differences between the point clouds are evident. These differences increase towards the left and right edges of the dam due to longer measurement distances. Since many CPs have a stronger influence at higher elevations (see Equations 2-4), systematic deviations also become more pronounced along the upper edge of the dam. The smallest deviations occur in the region of the change of faces, although a reversal in the sign of the differences can be observed there.

Distinct systematic patterns are also evident in the histogram of the M3C2 distances shown in Figure 6. After calibration, the M3C2 distances are expected to follow a normal distribution

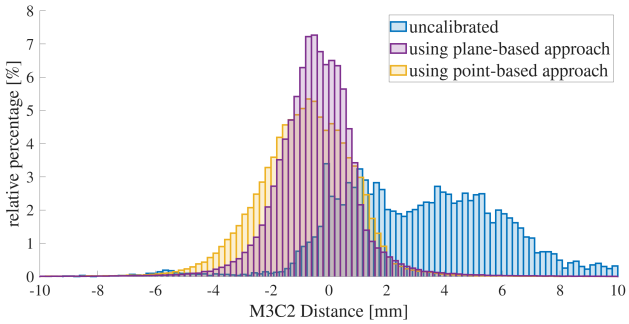

Figure 6. Histogram of M3C2 differences of measured point clouds at the water dam in front and back-face of the uncalibrated point cloud and the calibrated point cloud using plane-based and point-based approach.

	$\bar{x}_{M3C2}$ $[mm]$	s_{M3C2} $[mm]$
uncalibrated	3.1	–
calibrated plane-based (NIST)	−0.4	1.4
calibrated point-based (NIST)	−0.7	1.6
calibrated plane-based (Chow et al. (2011))	1.3	2.6

Table 4. Mean $\bar{x}_{M3C2}$ and standard deviations s_{M3C2} of M3C2 front- and back-face comparisons for uncalibrated and calibrated point clouds using plane- and point-based calibration using NIST model and model from Chow et al. (2011).

with a mean of $\bar{x}_{M3C2} = 0\ mm$ and a reduced standard deviation s_{M3C2}. The computed mean is given in Table 4. Since the assumption of a normal distribution does not apply, no standard deviation is provided. To evaluate the CPs obtained with the plane-based approach, we correct the point clouds of the water dam and repeat the M3C2 comparison. Figure 5b) shows the M3C2 distances after calibration. The distances are considerably reduced. Although some systematic patterns remain, their magnitudes are lower, with especially large deviations at the edges of the dam being significantly diminished. This demonstrates that the applied calibration effectively reduces systematic errors. The histogram of the M3C2 distances shown in Figure 6 supports this conclusion: it now closely resembles a normal distribution, and both the mean and standard deviation have decreased. A slight shift of the density distribution toward negative values indicates, however, that not all systematic effects have been completely removed.

We also carried out the M3C2 comparison using the calibrated point clouds derived from the well-established calibration field and the point-based approach. Figure 5c) presents the M3C2 distances along the dam, while Figure 6 shows the corresponding histogram. This method likewise results in a substantial reduction of systematic effects, although some systematic patterns remain visible.

A direct comparison of the histograms, together with their shape-describing parameters in Table 4, demonstrates that our calibration approach—despite yielding different numerical values of the CPs-reduces systematic effects in point clouds as effectively as the well-established point-based method in a calibration field. Although the CPs obtained from the plane-based approach exhibit higher standard deviations and correlations, the corrected point clouds show that our method achieves results comparable to those of the state-of-the-art approach. Importantly, our method does not require a dedicated, optimized calibration field.

To minimize systematic errors arising from the temporal instability of the CPs, the calibration measurements and the dam measurements were carried out only one day apart. Nonetheless, due to this short time interval and the transport of the TLS, some residual systematic deviations may persist.

5. Conclusion and Outlook

In this work, we presented a self-calibration method for panoramic Terrestrial Laser Scanners based on the calibration model introduced by the National Institute of Standards and Technology, and thus represents an extension of existing methods. Our approach does not require any additional measuring equipment, such as artificial targets; instead, it relies solely on planar patches extracted directly from the point clouds of the measurement environment. Using this approach, we are able to determine 14 of the 18 possible CPs of the NIST model.

By comparing our method with a state-of-the-art calibration approach and with independent measurements of a water dam, we demonstrate that our approach can reduce systematic effects in point clouds with comparable effectiveness. This holds true even though the estimated CPs exhibit higher standard deviations and correlations. Reduced calibration models that also use planar patches do not achieve this.

To ensure the comparability of the calibration results, the measurements for determining the CPs were not carried out directly on the actual measurement object. However, since our approach does not require any additional measuring equipment, it also enables on-site calibration directly on the object itself, provided that a sufficient number of planar structures are available. In future work, these structures could be identified automatically. Moreover, a hybrid approach that combines our plane-based method with the point-based method is conceivable. The main challenge in this case would be the weighting of the observations, as the number of individual point observations would be significantly smaller, but their precision considerably higher.

Overall, the quality of the computed CPs obtained with the plane-based method strongly depends on the relative orientation, number, size, and planarity of the selected patches. These patches should be arranged so that the CPs influence the observations as different as possible from the used stations, thereby maximizing sensitivity. Identifying planar patches that further enhance the sensitivity of the adjustment will be addressed in future work. In this context, it will also be analyzed whether a modified measurement geometry enables the estimation of the four remaining parameters or whether additional measurements of targets or normals would be required.

While reduced calibration models were shown to be less effective, further investigation is needed to identify the truly relevant parameters and their dependence on the specific scanner.

Acknowledgements

This research was funded by German Research Foundation (DFG) under grant number 490989047, ”Research Unit 5455 Deformation analysis based on terrestrial laser scanner measurements (TLS-Defo)”.

References

Abbas, M. A., Lichti, D. D., Chong, A. K., Setan, H., Majid, Z., 2014. An on-site approach for the self-calibration of terrestrial laser scanner. *Measurement*, 52, 111-123.

Besl, P. J., McKay, N. D., 1992. Method for registration of 3-d shapes. *Sensor fusion IV: control paradigms and data structures*, 1611, Spie, 586–606.

Chow, J. C. K., Lichti, D. D., Glennie, C., 2011. Point-Based Versus Plane-Based Self-Calibration of Static Terrestrial Laser Scanners. *The International Archives of the Photogrammetry, Remote Sensing and Spatial Information Sciences*, XXXVIII-5/W12, 121–126. https://isprs-archives.copernicus.org/articles/XXXVIII-5-W12/121/2011/.

Holst, C., Artz, T., Kuhlmann, H., 2014. Biased and Unbiased Estimates Based on Laser Scans of Surfaces with Unknown Deformations. *Journal of applied geodesy*, 8(3).

Holst, C., Kuhlmann, H., 2016. Challenges and present fields of action at laser scanner based deformation analyses. *Journal of applied geodesy*, 10(1), 17–25.

Janßen, J., Medic, T., Kuhlmann, H., Holst, C., 2019. Decreasing the Uncertainty of the Target Center Estimation at Terrestrial Laser Scanning by Choosing the Best Algorithm and by Improving the Target Design. *Remote Sensing*, 11, 845.

Jost, B., Coopmann, D., Holst, C., Kuhlmann, H., 2023. Real movement or systematic errors?–TLS-based deformation analysis of a concrete wall. *Journal of Applied Geodesy*, 17(2), 139–149.

Koch, K.-R., 2013. *Parameter estimation and hypothesis testing in linear models*. Springer Science & Business Media.

Koller, E., Jost, B., Kuhlmann, H., 2025. Towards the calibration of terrestrial laser scanners – a case study at a water dam. Technical report, Institute for Geodesy and Geoinformation.

Kotsakis, C., 2004. The effect of an unknown data bias in least-squares adjustment: some concerns for the estimation of geodetic parameters. *Newton’s bulletin (Print)*, 66–76.

Lichti, D. D., 2007. Error modelling, calibration and analysis of an AM–CW terrestrial laser scanner system. *ISPRS journal of photogrammetry and remote sensing*, 61(5), 307–324.

Lichti, D. D., 2010. Terrestrial laser scanner self-calibration: Correlation sources and their mitigation. *ISPRS Journal of Photogrammetry and Remote Sensing*, 65(1), 93-102.

Medić, T., Kuhlmann, H., Holst, C., 2019a. Automatic In-Situ Self-Calibration of a panoramic TLS from a single Station using 2D Keypoints. *ISPRS Annals of the Photogrammetry, Remote Sensing and Spatial Information Sciences*, IV-2/W5, 413–420. https://isprs-annals.copernicus.org/articles/IV-2-W5/413/2019/.

Medić, T., Kuhlmann, H., Holst, C., 2019b. Designing and evaluating a user-oriented calibration field for the target-based self-calibration of panoramic terrestrial laser scanners. *Remote Sensing*, 12(1), 15.

Medić, T., Kuhlmann, H., Holst, C., 2020. Empirical evaluation of terrestrial laser scanner calibration strategies: manufacturer-based, target-based and keypoint-based. *Contributions to International Conferences on Engineering Surveying: 8th INGEO International Conference on Engineering Surveying and 4th SIG Symposium on Engineering Geodesy*, Springer, 41–56.

Medić, T., Kuhlmann, H., Holst, C., 2021. A priori vs. in-situ terrestrial laser scanner calibration in the context of the instability of calibration parameters. *Contributions to International Conferences on Engineering Surveying: 8th INGEO International Conference on Engineering Surveying and 4th SIG Symposium on Engineering Geodesy*, Springer, 128–141.

Muralikrishnan, B., Ferrucci, M., Sawyer, D., Gerner, G., Lee, V., Blackburn, C., Phillips, S., Petrov, P., Yakovlev, Y., Astrelin, A. et al., 2015. Volumetric performance evaluation of a laser scanner based on geometric error model. *Precision Engineering*, 40, 139–150.

Muralikrishnan, B., Wang, L., Rachakonda, P., Sawyer, D., 2018. Terrestrial laser scanner geometric error model parameter correlations in the Two-face, Length-consistency, and Network methods of self-calibration. *Precision Engineering*, 52, 15–29.

Qiao, J., Butt, J. A., 2023. Self-calibration of terrestrial laser scanner using a M3C2-based planar patch algorithm. *ISPRS journal of photogrammetry and remote sensing*, 197, 335–345.

Reshetyuk, Y., 2009. Self-calibration and direct georeferencing in terrestrial laser scanning. PhD thesis, KTH.

Schwarz, W., 2018. *Ingenieurgeodäsie: Handbuch der Geodäsie, herausgegeben von Willi Freeden und Reiner Rummel*. Springer.

Shi, S., Muralikrishnan, B., Sawyer, D., 2020. Terrestrial laser scanner calibration and performance evaluation using the network method. *Optics and lasers in engineering*, 134, 106298.

Soudarissanane, S., Lindenbergh, R., Menenti, M., Teunissen, P., 2011. Scanning geometry: Influencing factor on the quality of terrestrial laser scanning points. *ISPRS journal of photogrammetry and remote sensing*, 66(4), 389–399.

Teng, J., Shi, Y., Wang, H., Wu, J., 2022. Review on the Research and Applications of TLS in Ground Surface and Constructions Deformation Monitoring. *Sensors*, 22(23). https://www.mdpi.com/1424-8220/22/23/9179.

Torr, P. H., Zisserman, A., 2000. MLESAC: A new robust estimator with application to estimating image geometry. *Computer vision and image understanding*, 78(1), 138–156.

Vosselman, G., Maas, H.-G., 2010. *Airborne and terrestrial laser scanning*. Whittles Publishing, Dunbeath, Scotland.

Wang, L., Muralikrishnan, B., Rachakonda, P., Sawyer, D., 2017. Determining geometric error model parameters of a terrestrial laser scanner through two-face, length-consistency, and network methods. *Measurement Science and Technology*, 28(6), 065016.

Weinmann, M., Jutzi, B., Mallet, C., 2014. Semantic 3D scene interpretation: A framework combining optimal neighborhood size selection with relevant features. *ISPRS Annals of the Photogrammetry, Remote Sensing and Spatial Information Sciences*, II-3, 181–188. https://isprs-annals.copernicus.org/articles/II-3/181/2014/.